

Cite this: DOI: 00.0000/xxxxxxxxxx

# Local Structure and Lithium Ion Diffusion Pathway of Cubic $\text{Li}_7\text{La}_3\text{Zr}_2\text{O}_{12}$ Studied by Total Scattering and the Reverse Monte Carlo Method<sup>†</sup>

Haolai Tian,<sup>\*,a</sup> Xiang Yang Kong,<sup>b</sup> Guanqun Cai,<sup>c</sup> Lei Tan,<sup>c</sup> Anthony E Phillip,<sup>c</sup> Isaac Abrahams,<sup>d</sup> David A Keen,<sup>e</sup> Dean Keeble,<sup>f</sup> and Martin T. Dove,<sup>g,h,‡</sup>

Received Date

Accepted Date

DOI: 00.0000/xxxxxxxxxx

The lithium-bearing oxide  $\text{Li}_7\text{La}_3\text{Zr}_2\text{O}_{12}$  (LLZO), with the cubic garnet crystal structure, is an excellent candidate for solid electrolytes with its structural stability and high  $\text{Li}^+$  conductivity. Here we use neutron and x-ray total scattering methods with the Reverse Monte Carlo method to identify the temperature-dependence of the  $\text{Li}^+$  distribution and of the stability and flexibility of the basic oxide structure. We compare with the results with the outcomes from supporting molecular dynamics simulations. The results give insight into the mechanism of  $\text{Li}^+$  conductivity.

## 1 Introduction

Lithium ion batteries have wide application on electric vehicles, mobile devices, and battery farms for renewable energy storage. However the commonly used liquid-based electrolytes have disadvantages such as flammability, volatile and operating temperature limitations. Although all-solid-state lithium ion batteries (SSLBs) which are expected to enhance the safety reliability and performance issues have been long sought, the conductivity of solid electrolytes can not keep competing at the level of the existed liquid-based counterpart.

Most solid electrolytes require both high  $\text{Li}^+$  conductivity and negligible electronic conductivity. However, in many materials the requirement to match high ionic conductivity with high electrochemical stability for commercialised battery applications is problematic. Recently the lithium-containing oxide  $\text{Li}_7\text{La}_3\text{Zr}_2\text{O}_{12}$  (LLZO)<sup>1–3</sup>, which crystallises with the cubic garnet structure, has

attracted much attention as a potential solid electrolyte because it has both high  $\text{Li}^+$  conductivity and is stable against chemical reaction with Li metal, moisture, air, as well as being able to support both low and high electrical potential differences.

LLZO actually exists in two phases<sup>4</sup>, of cubic and tetragonal symmetry, and the two phases show different  $\text{Li}^+$  conductivities. The conductivity of the cubic phase is two orders of magnitude higher than tetragonal one,  $3 \times 10^{-4} \text{ S/cm}^1$  and  $1.63 \times 10^{-6} \text{ S/cm}^5$ , respectively. This difference may be related to the distances between Li sites, disorder degree of Li atom, and isotropic diffusion pathways in the cubic phase.

A cubic garnet structure can be described<sup>6</sup> as having a general chemical formula of the form  $\text{A}_3\text{B}_2(\text{TO}_4)_3$ , where the T site has tetrahedral coordination with oxygen (24 sites in the cubic unit cell), the B site has octahedral coordination (16 sites in the unit cell), and the larger A site has 8-fold coordination (24 sites in the unit cell). In LLZO the  $\text{Zr}^{4+}$  cations are in the B sites, and the  $\text{La}^{3+}$  cations are in the A site. The tetrahedral sites are occupied by  $\text{Li}^+$  cations, but full occupancy would only accommodate 3 of the 7 cations of the chemical formula. In crystal structure refinements, sites of general symmetry and irregular coordination with oxygen atoms are associated with the positions of the remaining  $\text{Li}^+$  cations. However, there are 96 of these sites, and therefore there must only be partial occupancy in this model. Indeed, with more than one position available to the  $\text{Li}^+$  cations there is no reason why the tetrahedral sites should be fully occupied, and this partial occupancy is what allows for three-dimensional ionic conductivity.

The atomic structure of LLZO has been studied by two complementary methods. The first is standard crystallography, with both x-ray<sup>4,5,7–11</sup> and neutron<sup>5,7,9,12–15</sup> beams, from which  $\text{Li}^+$  sites can be identified and their site occupancies refined. Using

<sup>a</sup> China Spallation Neutron Source (CSNS), Institute of High Energy Physics (IHEP), Chinese Academy of Sciences (CAS), Dongguan 523803, People's Republic of China

<sup>b</sup> School of Materials Sciences and Engineering, Shanghai Jiao Tong University, Huashan Road 1954, Shanghai 200030, People's Republic of China

<sup>c</sup> School of Physics and Astronomy, Queen Mary University of London, Mile End Road, London, E1 4NS, United Kingdom

<sup>d</sup> School of Biological and Chemical Sciences, Queen Mary University of London, Mile End Road, London, E1 4NS, United Kingdom

<sup>e</sup> ISIS Neutron and Muon Facility, Rutherford Appleton Laboratory, Harwell Campus, Didcot, Oxfordshire, OX11 0QX, United Kingdom

<sup>f</sup> Diamond Light Source Ltd, Harwell Science and Innovation Campus, Didcot, OX11 0DE, United Kingdom

<sup>g</sup> College of computer science, Sichuan University, Chengdu, 610065, People's Republic of China

<sup>h</sup> School of Physics, School of Sciences, Wuhan University of Technology, Wuhan, Hubei 430070, People's Republic of China

<sup>‡</sup> Corresponding author. email: martin.dove@icloud.com

a maximum entropy method it was possible to visualise the  $\text{Li}^+$  diffusion pathway<sup>13</sup>. The second method is molecular dynamics simulation<sup>15,16</sup>, which has given results broadly consistent with the crystal structure refinements.

In this paper we use the methods of neutron and synchrotron x-ray total scattering methods together with the Reverse Monte Carlo (RMC) method to create an image of the  $\text{Li}^+$  site disorder for a wide range of temperatures. The X-ray data are sensitive to the atomic numbers, which means that the data for x-ray total scattering will be mostly sensitive to the  $\text{La}^{3+}$  and  $\text{Zr}^{4+}$  cations, and to a lesser extent to the  $\text{O}^{2-}$  anions, but will have virtually no sensitivity to the  $\text{Li}^+$  cations. On the other hand, neutron total scattering will have enhanced sensitivity to the  $\text{O}^{2-}$  anions and, but to a lesser extent also, to the  $\text{Li}^+$  cations. The combination of the two techniques will give greater chance to identify the spatial distribution of the  $\text{Li}^+$  cations.

## 2 Experimental methods

### 2.1 Synthesis

The precursor materials used were anhydrous  $\text{LiOH}$  (Alfa Aesar 99.5%, dried at 200 °C overnight; 10 wt.% excess was taken to compensate for the loss of lithium under annealing conditions),  $\text{La}_2\text{O}_3$  (Alfa Aesar, treated at 950 °C overnight),  $\text{ZrO}_2$  (Alfa Aesar, 99.7%). The reactants were mixed with a mortar and pestle before reacting them at 950 °C for 12 hours. The resultant product was reground and pressed into pellets. The pellets were transferred to an alumina crucible and buried with mother powder, followed by sintering at 1140 °C for 20 hours to form single-phase material. The resulting pellets were ground into powder and stored in an argon-filled glovebox ( $<0.1$  ppm  $\text{O}_2$ ,  $<0.1$  ppm  $\text{H}_2\text{O}$ ) to prevent reaction with humidity.

### 2.2 Neutron Powder Diffraction and Total Scattering

Neutron powder diffraction and total scattering data were obtained at a number of temperatures on the GEM diffractometer<sup>17</sup> at the ISIS spallation neutron source, Rutherford Appleton Laboratory, UK. The LLZO sample was contained in a cylindrical thin-walled vanadium can of 8 mm diameter. This was mounted in a standard vanadium-foil furnace for measurements at and above room temperature (at 293 K, 450 K, 600 K, 750 K, 900 K and 1100 K). Data were collected on six separate occasions, counting for between 5 and 6 hours per temperature.

Measurements were also performed on the empty instrument, the empty furnace, and an empty vanadium can within the furnace to account for experimental background scattering and sources of beam attenuation, and also of an 8 mm diameter vanadium rod for normalisation. The data were processed using the GudrunN software<sup>18</sup> to obtain the scattering data and pair distribution function as described below, with a maximum scattering vector of  $Q_{\text{max}}$  of 50  $\text{\AA}^{-1}$ . Diffraction data were also corrected and reduced using the Mantid software<sup>19</sup>. Rietveld refinement of the crystal structures was performed by GSAS software<sup>20</sup> with the EXPGUI interface<sup>21</sup>.

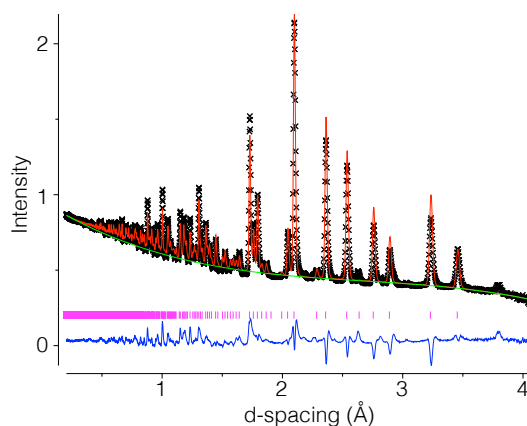


**Fig. 1** Example of the quality of the Rietveld refinement of the crystal structure of LLZO from data collected from the 60° (Bank 4) at temperature of 293K.

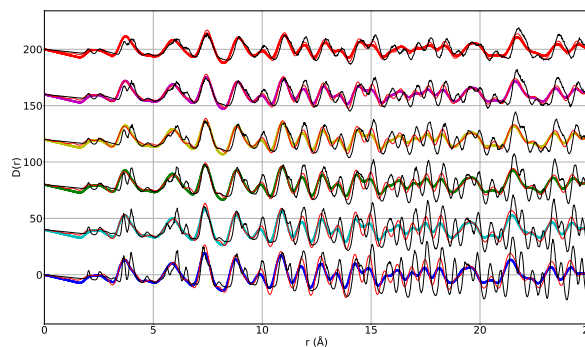


**Fig. 2** Synchrotron pair distribution  $D(r)$  obtained from GudrunX for all temperatures represented as circles. A constant offset has been applied to separate those curves. The solid black lines indicate the simulated intensities from DI\_poly, and RMC modelling are represented by the solid red lines.

### 2.3 Synchrotron Total Scattering

Synchrotron powder diffraction and total scattering data were collected on the XPDF beamline (I15-1 instrument) at Diamond Light Source (UK). The X-rays were monochromatized to give a wavelength of 0.161669  $\text{\AA}$ . The sample was sealed into borosilicate capillary tubes ( $\phi$  1 mm, and 50 mm in length) for measurements at the same temperatures as the neutron beam measurements. The raw data were corrected and reduced into scattering data using the program DAWN<sup>22</sup>. And PDF  $D(r)$  were processed from scattering data using GudrunX<sup>18,23</sup> with the range of data between  $0.5 \leq Q \leq 25 \text{ \AA}^{-1}$  for the Fourier transformation. Corrections for fluorescence were applied, in which the fluorescence energy of La was assumed to be 38.739 keV.

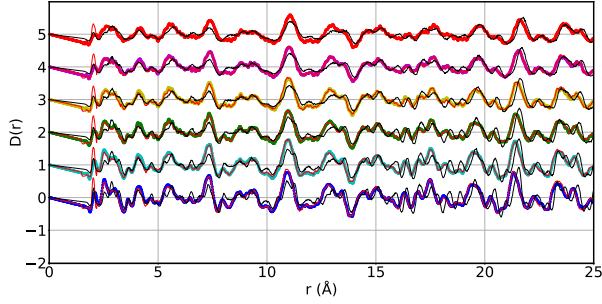


**Fig. 3** Neutron pair distribution  $D(r)$  obtained from GudrunN for all temperatures represented as circles. A constant offset has been applied to separate those curves. The solid black lines indicate the simulated intensities from DI\_poly, and RMC modelling are represented by the solid red lines.

## 2.4 Pair Distribution Function

The differential cross section for the scattering of a beam of radiation as integrated over all changes of energy is defined as

$$\frac{1}{N} \frac{d\sigma}{d\Omega} = I(Q) = I^S(Q) + i(Q) \quad (1)$$

where  $I^S(Q) = \sum_m c_m f_m^2$  is the self-scattering of all atoms,  $c_m$  is the fractional amount of atom type  $m$  such that  $\sum_m c_m = 1$ , and  $f_m$  is the scattering factor of atom of type  $m$  (the symbol  $b_m$  is usually used for neutron scattering, denoting the scattering length whose value is independent of  $Q$ )<sup>24</sup>. The function  $i(Q)$  is the total scattering structure factor. Here we define the partial pair distribution function (PDF)  $g_{mn}(r)$  to represent the number of atoms of type  $n$  within the shell between  $r$  and  $r + dr$  centred on a particle of type  $m$ , namely of value  $4\pi r^2 dr \times c_n \rho \times g_{mn}(r)$ , where  $\rho$  is the overall atomic number density. The structure factor  $i(Q)$  can then be written as<sup>25</sup>

$$i(Q) = 4\pi\rho \int_0^\infty \sum_{m,n} c_m c_n f_m f_n r^2 [g_{mn}(r) - 1] \frac{\sin Qr}{Qr} dr \quad (2)$$

The overall pair distribution function is defined as

$$D(r) = 4\pi\rho r \sum_{m,n} c_m c_n f_m f_n [g_{mn}(r) - 1] \quad (3)$$

so that

$$Qi(Q) = \int_0^\infty D(r) \sin Qr dr \quad (4)$$

In turn, the function  $D(r)$  can be obtained as the the sine Fourier transform of  $Qi(Q)$ , but in practice the transform is modified as

$$D(r) = \frac{2}{\pi} \int_0^{Q_{\max}} M(Q) Qi(Q) \sin Qr dr \quad (5)$$

where  $M(Q) = \sin(\pi Q/Q_{\max})/(\pi Q/Q_{\max})$  is the Lorch function, which is introduced to reduce the effect of finite maximum momentum transfer,  $Q_{\max}$ <sup>25–27</sup>. Those tasks were carried out using the programs GudrunX and GudrunN<sup>18,23</sup>.

**Table 1** The minimum distances between pairs of atoms

	Li	O	Zr	La
Li	1.69	1.50	2.3	2.3
O		2.2	1.79	2.2
Zr			5.0	3.3
La				3.3

## 2.5 Reverse Monte Carlo Analysis

The Reverse Monte Carlo (RMC) method, whilst initially developed for the study of highly-disordered (non-crystalline) materials<sup>28</sup>, is in fact an excellent technique for the study of disordered crystalline materials<sup>29</sup>. That said, it appears that there have been only limited applications of the RMC method to crystalline fast-ion conductors<sup>30–33</sup>, and apparently not to the cases where lithium is the mobile ion. We will comment later on some observations on the application of the RMC method to lithium fast-ion conductors in the light of the experience gained in this study.

The RMC method is a way to visualise the atomic-scale structure of a material through a simulation based on experimental data. It uses a Monte Carlo method to minimise the difference between experimental functions and the values computed from the atomic configuration as expressed in the function

$$\chi^2 = \sum_j \sum_i (y_{i,j}^{\text{obs}} - y_{i,j}^{\text{calc}})^2 / \sigma_j^2 \quad (6)$$

where  $y_{i,j}^{\text{obs}}$  is the observed values at data point  $i$  in data set  $j$ ,  $y_{i,j}^{\text{calc}}$  is the calculated counterpart, and  $\sigma_j^2$  is weighing function that may represent the statistical accuracy of data set. In this study, the data sets used include  $i(Q)$  from both neutron and synchrotron power diffraction,  $D(r)$  from the neutron total scattering data, and the Bragg data from the neutron diffraction measurements. In the RMC method an selected at random is moved by a random amount up to a specified maximum. The move is accepted if the value of  $\chi^2$  is lowered. On the other hand, if the value of  $\chi^2$  increases by an amount  $\Delta\chi^2$ , the move is accepted only with probability  $\exp(-\Delta\chi^2/2)$ . Each simulation ran until the value of  $\chi^2$  had reached a stable minimum value, corresponding in this case to around 300 accepted moves per atom.

The RMC simulations were performed using the program RMCprofile v6.7<sup>34</sup>. The starting configurations of  $\text{Li}_7\text{La}_2\text{Zr}_3\text{O}_{12}$  were generated from the results of Rietveld refinement using the data2config/RMCcreate program<sup>35</sup>. Configurations were  $4 \times 4 \times 4$  supercell of the conventional body-centred unit cell with linear dimension of around 52 Å, containing 12288 atoms. Maximum atomic moves of La, O and Zr atoms were of size 0.05, but those of Li were 0.1. Minimum distance constraints were applied within the RMC simulation; between pairs of atoms as given in Table 1. Finally, bond-stretching and bond-bending potentials were applied within the  $\text{ZrO}_6$  octahedra, and for the La–O bonds, during the RMC simulation.

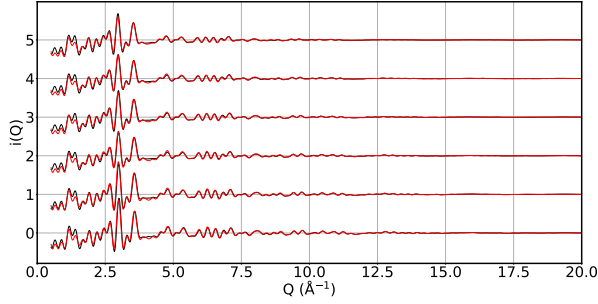


**Fig. 4** Neutron scattering function  $S(Q)$  for all temperatures. A constant offset has been applied to separate those curves.

## 2.6 Electrochemical Impedance Measurements

Electrochemical experiments were carried out in an Ar glovebox ( $O_2$ ;  $H_2O < 1$  ppm). For the electrical measurement, gold electrodes were evaporated on LLZO by thermal evaporation. The EIS was recorded by a Solartron ModuLab system, and contacted via a probe station on a hot stage in the glovebox. EIS was performed with an 10 mV amplitude voltage in a frequency range of 50 mHz to 1 MHz.

## 2.7 Molecular Dynamic Simulation

Classical molecular dynamics (MD) simulations were performed using the DL\_POLY package<sup>36</sup>. Empirical force-fields were used, which include the long-range Coulomb potential, short-range Buckingham potential functions to describe the energy between two ions of type  $m$  and  $n$ ,  $E_{mn}(r)$ , assumed to be functions of inter-ionic separation  $r$  only:

$$E_{mn}(r) = \frac{Q_m Q_n}{4\pi\epsilon_0 r} + A_{mn} \exp(-r/\rho_{mn}) - C_{mn} r^{-6} \quad (7)$$

with ions treated as rigid entities with no induced polarisation, and assigned formal charges,  $Q_{Zr} = +4e$ ,  $Q_{La} = +4e$ ,  $Q_{Li} = +e$ ,  $Q_O = -2e$ , where  $e$  is the positive unit charge value. The parameters of the force-field were taken from the work of Wang et al<sup>15</sup>, who used a combination of literature and new values; the parameters of the force field are given in Table 2. The starting configurations were the same as used in the RMC work (linear dimensions of around 52 Å, and 12288 atoms), and simulations were performed at the same temperatures as in the neutron and x-ray total scattering measurements.

Simulations were performed within thermodynamic ensembles that were either constant-stress<sup>37,38</sup> and constant temperature<sup>39,40</sup>, or the standard constant-volume constant-energy microcanonical conditions. Simulations were performed using a time step of 0.001 ps, allowing 5 ps for equilibration.

# 3 Results and discussion

## 3.1 Crystal Structure Analysis

The structural parameters of Rietveld refinement for all temperatures are listed in Table 3, which fitted well to the cubic model with space group  $Ia\bar{3}d$ . A sample fit to the data, namely for the

**Table 2** Force-field parameters for the molecular dynamics simulations, from the work of Wang et al<sup>15</sup>, with interactions between cations assumed to be give only by the Coulomb interaction. Ions are assigned their formal charge values. The parameters are defined by equation 7.

	$A$ (eV)	$\rho$ (Å)	$C$ (eV Å <sup>6</sup> )
Zr-O	1385.02	1.79	0
La-O	4579.23	0.3044	0
Li-O	632.102	0.2906	0
O-O	22764.30	0.1490	27.63

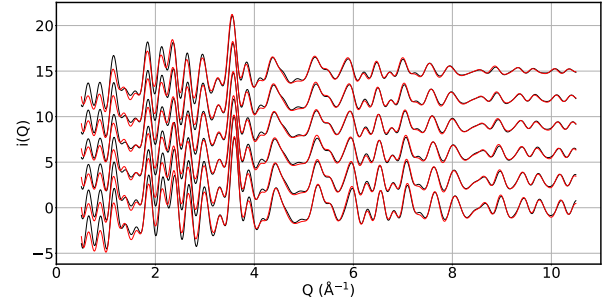


**Fig. 5** Synchrotron scattering function  $S(Q)$  for all temperatures. A constant offset has been applied to separate those curves.

data at 293 K, is shown in Fig. 1 The lattice parameters are plotted as functions of temperature in Fig. 6, showing a linear thermal expansion. The coefficient of volumetric thermal expansion is  $\alpha_V = 1.18 \times 10^{-5} K^{-1}$ . The structure is in good agreement with previous structure refinements<sup>4,5,7-15</sup>; aspects of the crystal structure have been discussed in these previous works.

## 3.2 Local Structure Analysis

The synchrotron pair distribution function  $D(r)$  defined as functions 3 and 5, are shown in Fig. 2. The first peak corresponds to the La-O nearest-neighbor distance at around 2.5 Å, and the second peaks refers to La-Zr around 3.6 Å. The position and integrated area are constant for all temperatures, reflection there is no significant differences in crystal framework structure. The higher- $r$  PDF shows shifting and broadening of the peaks as the temperature rising, because of the increases of the lattice parameters.

The RMC analysis used 4 data sets to perform RMC fits, including Bragg data (Fig.7) and PDF  $D(r)$  from neutron total scattering (Fig.3), and scattering function  $i(Q)$  from both neutron (Fig.4) and synchrotron experiments(Fig.5) .

The low- $r$  distributions of distances from the RMC and MD configurations are shown in Fig.8 and Fig.9. The interesting point about these diagrams is that the Li-X (X represents Li, La, Zr or O) distribution from RMC are smoother than those from MD in all temperatures, as shown in Fig.8, indicating the Li-ion movement remains disorderly. But the framework structure keep stable in each case as shown in Fig.9, which is consist with the result of XPDF as shown in Fig. 2.

**Table 3** Lattice parameters, atomic fractional coordinates and Lithium site occupancy of  $\text{Li}_7\text{La}_2\text{Zr}_3\text{O}_{12}$  obtained from Rietveld refinement. Zr has fractional coordinates 0,0,0, La has fractional coordinates 1/4,0,1/4,  $\text{Li}_1$  has fractional coordinates 3/8,0,1/4, and  $\text{Li}_2$  has fractional coordinates 1/4,y,z. Standard deviations are given for the last significant figures in brackets.

T (K)	a (Å)	O (x)	O (y)	O (z)	$\text{Li}_1$ occ.	$\text{Li}_2$ (y)	$\text{Li}_2$ (z)
273	12.921268(90)	0.102208(76)	0.196891(77)	0.281292(67)	0.3(1)	0.17673(37)	0.42673(37)
450	12.952687(88)	0.102172(76)	0.196875(76)	0.281281(67)	0.3(1)	0.17769(36)	0.42769(36)
600	12.979779(70)	0.102361(63)	0.197156(64)	0.280766(56)	0.3(1)	0.17872(28)	0.42872(28)
750	13.008921(92)	0.102281(81)	0.197353(82)	0.281026(72)	0.3(1)	0.17725(38)	0.42725(38)
900	13.03568(17)	0.10271(14)	0.19765(15)	0.28036(14)	0.3(1)	0.17527(74)	0.42527(74)
1100	13.08621(10)	0.102407(99)	0.19791(10)	0.280357(89)	0.3(1)	0.17683(18)	0.42683(18)

**Table 4** Li displacement parameters  $100 \times U_{ij}(\text{\AA}^2)$  refined from Rietveld refinement. For  $\text{Li}_2$   $U_{22} = U_{33}$  and  $U_{12} = -U_{13}$ .  $U_{ij}$  units are in  $\text{\AA}^2$ . Standard deviations are given for the last significant figures in brackets.

T (K)	$\text{Li}_1$ $U_{\text{iso}}$	$\text{Li}_2$ $U_{11}$	$\text{Li}_2$ $U_{22}$	$\text{Li}_2$ $U_{12}$	$\text{Li}_2$ $U_{23}$
273	-0.307(40)	26.3(11)	4.77(40)	-11.67(51)	-4.86(43)
450	0.80(35)	21.0(14)	2.91(39)	-7.99(57)	-3.27(41)
600	6.51(46)	24.7(11)	4.96(43)	-8.90(47)	-3.77(40)
750	2.06(81)	25.0(20)	4.82(62)	-12.49(98)	-5.97(63)
900	34.3(61)	16.3(30)	1.74(77)	-7.8(13)	-3.00(76)
1100	-3.15(18)	23.6(18)	-1.35(28)	-2.71(51)	-3.07(29)

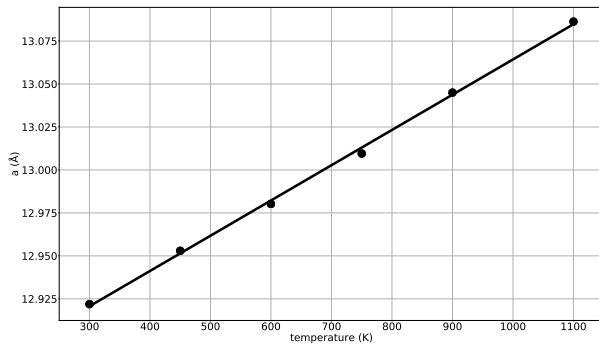


**Fig. 6** Variation of the lattice parameter of  $\text{Li}_7\text{La}_2\text{Zr}_3\text{O}_{12}$  with temperature as obtained by Rietveld analysis (Table 3).

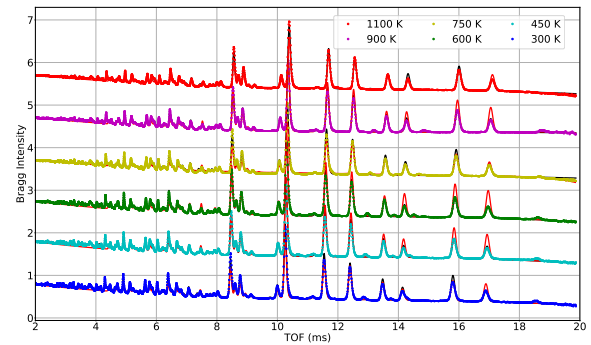


**Fig. 7** The Bragg diffraction data. The data are represented as circles with constant offset to separate those curves. The solid black lines indicate the calculated intensities from GSAS, and RMC modeling are represented by the solid red lines.

### 3.3 Electrochemical Impedance Spectroscopy

The EIS of the LLZO were examined with a in-plane geometry at elevated temperatures from  $-20^\circ\text{C}$  to  $100^\circ\text{C}$ , as shown in Fig.10. From the Nyquist plots, a typical semi arc with the straight tail indicates the ion in-plane diffusion at low frequency occurs along the LLZO. The ion conductivity is about  $2.1 \times 10^{-4}$  S/cm at room temperature.

The activation energy can be calculated from the series of EIS at elevated temperatures shown in Fig.11. The activation energy  $E_a$  is estimated based on the Arrhenius equation for the ionic conductivity

$$\sigma T = \sigma_0 e^{-E_a/k_B T} \quad (8)$$

where  $\sigma$  is the ionic conductivity,  $\sigma_0$  is a pre-exponential factor, T is the absolute temperature, and  $k_B$  is the Boltzmann constant. Furthermore, the diffusion coefficient was calculated using the

Nernst-Einstein-equation

$$D = \frac{\sigma k_B T}{N_{\text{Li}} q^2} \quad (9)$$

where q is the charge of the lithium and  $N_{\text{Li}}$  the concentration of lithium, in this case for a cubic LLZO structure. The calculated activation energy is about 0.36 eV which is in good agreement to other publications, as well as the diffusion coefficient shown in Fig.12 with  $1.31 \times 10^{-13} \text{ m}^2\text{s}^{-1}$  at room temperature.

### 3.4 Lithium Distribution and Dynamics Analysis

The 3D density maps of Li in cubic garnets are shown in Fig.13. The lithium distribution can be expected in liquid and amorphous materials



**Table 5** Atomic (Except Li) displacement parameters  $100 \times U_{ij}$  ( $\text{\AA}^2$ ) refined from Rietveld refinement.  $U_{ij}$  units are in  $\text{\AA}^2$ . Standard deviations are given for the last significant figures in brackets.

T(K)	O $U_{11}$	O $U_{22}$	O $U_{33}$	O $U_{12}$	O $U_{13}$	O $U_{23}$	La $U_{\text{iso}}$	Zr $U_{\text{iso}}$ Li7
273	0.382(44)	1.017(52)	0.425(44)	-0.303(39)	-0.052(36)	0.261(38)	0.281(15)	0.240(22)
450	0.838(49)	1.266(57)	0.822(52)	-0.056(45)	-0.005(42)	0.177(43)	0.622(19)	0.599(27)
600	1.430(43)	2.357(52)	1.830(51)	-0.124(40)	0.096(39)	0.309(41)	1.168(17)	1.117(23)
750	1.238(60)	2.437(75)	1.653(72)	-0.448(56)	0.189(55)	0.471(58)	0.861(24)	0.636(30)
900	0.014(92)	1.25(12)	0.211(98)	-0.536(85)	-0.090(76)	0.414(86)	0.340(40)	0.083(50)
1100	1.199(73)	3.172(97)	1.941(88)	-0.041(70)	0.404(68)	0.189(73)	0.724(28)	0.404(34)

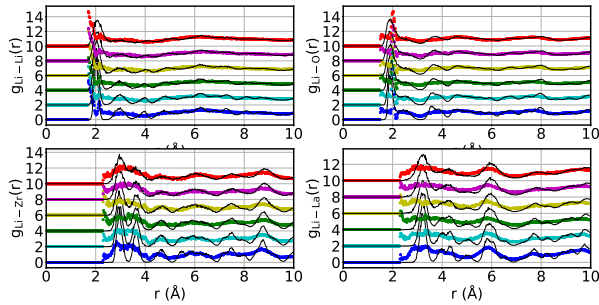


**Fig. 8** The distributions calculated from RMCProfile of (1) Li-Li, (2) Li-O, (3) Li-Zr, (4) Li-La at low- $r$  range for all temperatures. A constant offset has been applied to separate those curves.

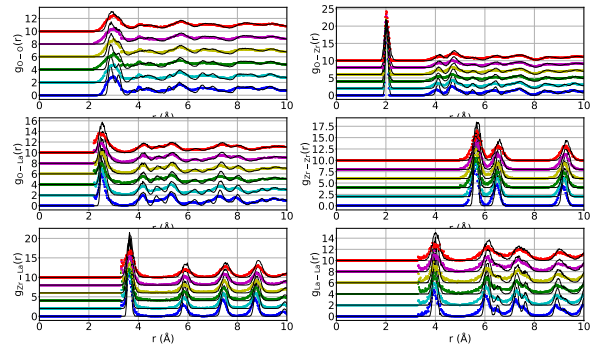


**Fig. 9** The distributions calculated from RMCProfile of (1) O-O; (2) O-Zr; (3) O-La; (4) Zr-Zr; (5) Zr-La; (6) La-La at low- $r$  range for all temperatures. A constant offset has been applied to separate those curves. The solid lines (black) indicate the values obtained from Molecular Dynamic simulation

## 4 Conclusions

The conclusions section should come in this section at the end of the article, before the Conflicts of interest statement.

## 5 Appendix

### 5.1 The Correlation Functions

Time-dependent correlation functions are valuable tools to describe the average way the quantity will change with time, and predict the trends within the behaviour of atomic structure and dynamics.

One of the simplest correlation function for velocity with a mean value of zero,  $C(t)$ , is defined as

$$C(t) = \frac{\langle v(0)v(t) \rangle}{\langle v(0)^2 \rangle} = \frac{(\lim_{\mathcal{T} \rightarrow \infty} \frac{1}{\mathcal{T}} \int_0^{\mathcal{T}} v(t')v(t+t')dt')}{\langle v^2 \rangle} \quad (10)$$

For the harmonic crystal, the velocity of the  $j$ -th atom is given as

$$v_j(t) = \frac{-i}{(Nm_j)^{1/2}} \sum_{\mathbf{k}, \nu} \omega(\mathbf{k}, \nu) \mathbf{e}_j(\mathbf{k}, \nu) \exp(i\mathbf{k} \cdot \mathbf{r}) Q(\mathbf{k}, \nu, t) \quad (11)$$

and leads to the classical result:

$$\sum_j m_j \langle |v_j(t) \cdot v_j(0)| \rangle = \frac{k_B T}{N} \sum_{\mathbf{k}, \nu} \cos(\omega(\mathbf{k}, \nu)t) \quad (12)$$

In addition, the power spectra  $Z(\omega)$  is given by the Fourier transform of  $C(t)$ :

$$Z(\omega) = \int C(t) \exp(-i\omega t) dt \quad (13)$$

It can be seen that the power spectrum of the mass-weighted velocity correlation function is equal to the phonon density of states.

Consider another correlation function for position of atom,  $G_s(r; t)$ , is defined as

$$\begin{aligned} G_s(\Delta r, t) &= \frac{\langle r(0)r(t) \rangle}{\langle |r(0)|^2 \rangle} \\ &= \frac{1}{N} \sum_j \int \langle \delta(r' - r_j(0)) \delta(r' + \Delta r - r_j(t)) \rangle dr' \\ &= \frac{1}{N} \langle \sum_j \delta(\Delta r + r_j(0) - r_j(t)) \rangle \end{aligned}$$

which is related to the probability of finding an atom in the volume  $dr$  at position  $\Delta r$  for a time interval of  $t$ , and can be named as self-part of van Hove correlation function.

The mean square displacement (MSD)  $\langle \Delta r_i(t)^2 \rangle$  is a measure of the deviation of the position of an atom with respect to a reference position over time. MSD is related to the  $G_s(r; t)$  as:

$$\langle \Delta r_i(t)^2 \rangle = \int_0^\infty \langle \Delta r_i(t)^2 \rangle \cdot 4\pi \langle \Delta r_i(t)^2 \rangle G_s(\Delta r, t) d\Delta r \quad (14)$$

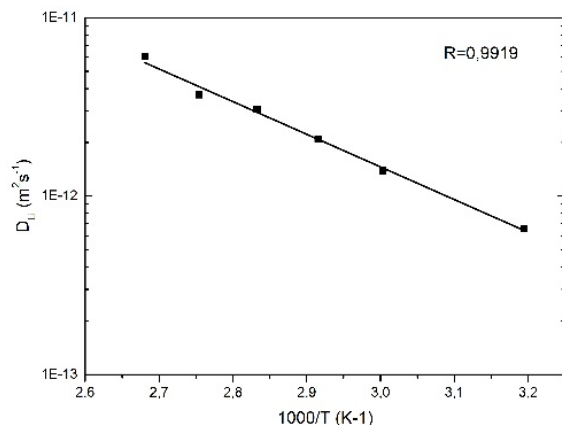


**Fig. 12** Diffusion coefficient at different temperatures

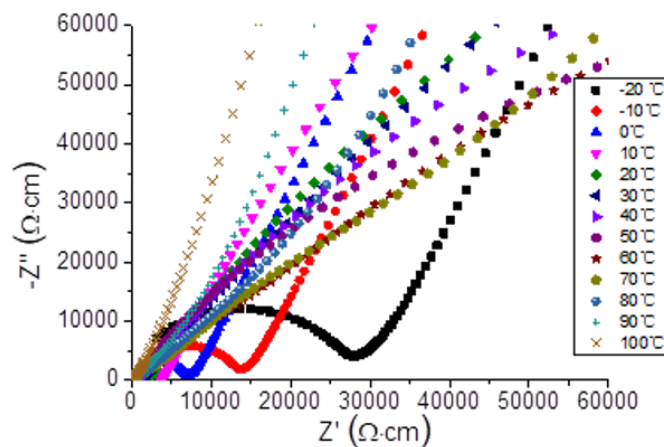


**Fig. 10** AC impedance data collected from -20°C to 100°C.

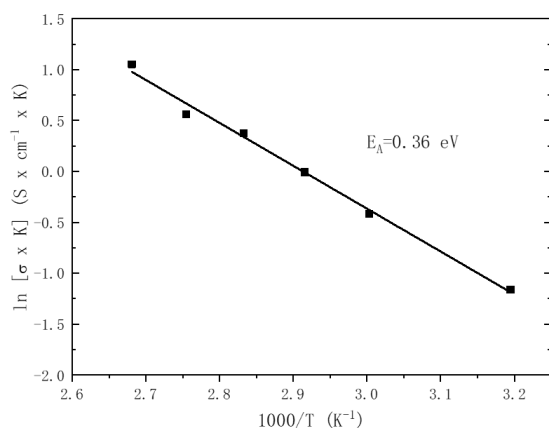


**Fig. 11** A plot of conductivity as a function of temperature for LLZO. The line indicates an Arrhenius fit over the whole temperature range.

## 5.2 Nernst-Einstein Equation

The value of ionic conductivity ( $\sigma$ ) is determined by the impedance spectroscopy. In solid electrolytes, as the anions are immobile, the ionic conduction is driven by the diffusion of  $\text{Li}^+$  ions. The connection between the diffusion constant ( $D$ ) and  $\sigma$  is defined by the Nernst-Einstein (NE) equation, which are widely used for electrolyte system. NE equation is given as

$$D(T) = \frac{kT}{Ne^2} \sigma(T) \quad (15)$$

where  $k$  is the Boltzmann constant,  $e$  is the elementary charge, and  $N$  is the number of carrier ions.

## Conflicts of interest

There are no conflicts to declare.

## Acknowledgements

The Acknowledgements come at the end of an article after Conflicts of interest and before the Notes and references.

## Notes and references

- 1 R. Murugan, V. Thangadurai and W. Weppner, *Angewandte Chemie International Edition*, 2007, **46**, 7778–7781.
- 2 A. J. Samson, K. Hofstetter, S. Bag and V. Thangadurai, *Energy & Environmental Science*, 2019, **12**, 2957–2975.
- 3 K. Kataoka, *Journal of the Ceramic Society of Japan*, 2020, **128**, 7–18.
- 4 C. A. Geiger, E. Alekseev, B. Lazic, M. Fisch, T. Armbruster, R. Langner, M. Fechtelkord, N. Kim, T. Pettke and W. Weppner, *Inorganic Chemistry*, 2011, **50**, 1089–1097.
- 5 J. Awaka, N. Kijima, H. Hayakawa and J. Akimoto, *Journal of Solid State Chemistry*, 2009, **182**, 2046–2052.
- 6 E. J. Cussen, T. W. S. Yip, G. O'Neill and M. P. O'Callaghan, *Journal of Solid State Chemistry*, 2011, **184**, 470–475.
- 7 H. Buschmann, J. D. O. lle, S. Berendts, A. Kuhn, P. Bottke, M. Wilkening, P. Heitjans, A. Senyshyn, H. Ehrenberg, A. Lotnyk, V. Duppel, L. Kienle and J. Janek, *Physical Chemistry Chemical Physics*, 2011, **13**, 19378–15.
- 8 J. Awaka, A. Takashima, K. Kataoka, N. Kijima, Y. Idemoto and J. Akimoto, *Chemistry Letters*, 2011, **40**, 60–62.
- 9 Daniel Rettenwander, G. J. Redhammer, F. Preishuber-Pflugl, L. Cheng, L. Miara, R. Wagner, A. Welzl, E. Suard, Marca M Doeff, M. Wilkening, J. Fleig and G. Amthauer, *Chemistry of Materials*, 2016, **28**, 2384–2392.
- 10 R. Wagner, G. J. Redhammer, D. Rettenwander, A. Senyshyn, W. Schmidt, M. Wilkening and G. Amthauer, *Chemistry of Materials*, 2016, **28**, 1861–1871.
- 11 K. Kataoka and J. Akimoto, *Journal of the Ceramic Society of Japan*, 2019, **127**, 521–526.
- 12 H. Xie, J. A. Alonso, Y. Li, M. T. Fernandex-Diaz and J. B. Goodenough, *Chemistry of Materials*, 2011, **23**, 3587–3589.
- 13 J. Han, J. Zhu, Y. Li, X. Yu, S. Wang, G. Wu, H. Xie, S. C. Vogel, F. Izumi, K. Momma, Y. Kawamura, Y. Huang, J. B. Goodenough and Y. Zhao, *Chemical Communications*, 2012, **48**, 9840–3.

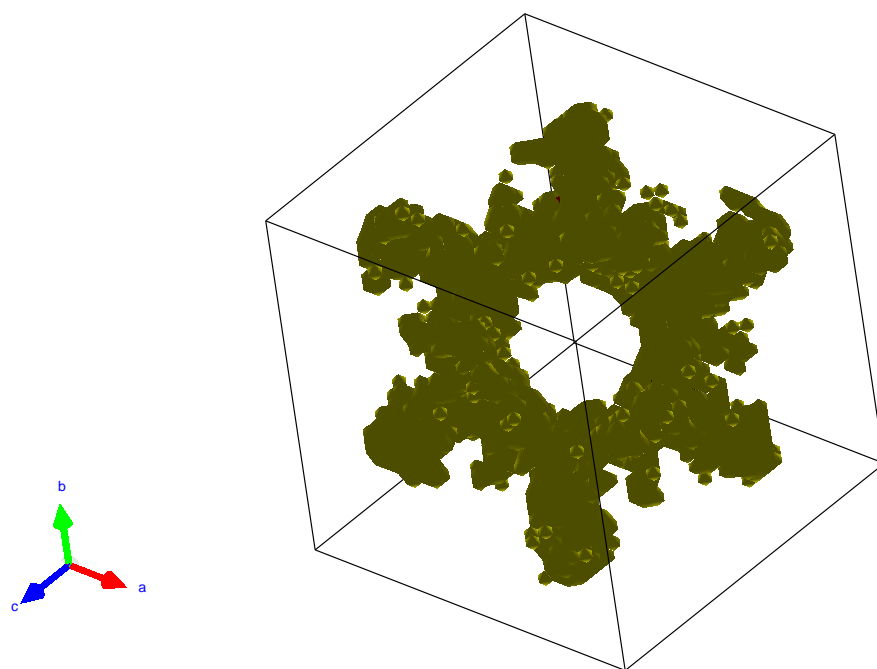


**Fig. 13** Isosurfaces with level of  $0.1 \text{ \AA}^{-3}$  (yellow) and  $3 \text{ \AA}^{-3}$  (red)

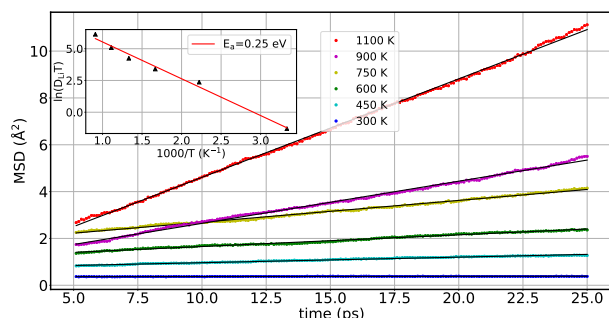


**Fig. 14** Mean squared displacement (MSD) of Li from 300 K to 1100 K. The slope of MSD of each temperature data set yields the diffusion constant ( $D$ ). The inset shows a diffusion constant ( $D$ ) versus temperatures.

- 14 Y. Li, J.-T. Han, C.-A. Wang, S. C. Vogel, H. Xie, M. Xu and J. B. Goodenough, *Journal of Power Sources*, 2012, **209**, 278–281.
- 15 Y. Wang, A. Huq and W. Lai, *Solid State Ionics*, 2014, **255**, 39–49.
- 16 M. Klenk and W. Lai, *Physical Chemistry Chemical Physics*, 2015, **17**, 8758–8768.
- 17 A. C. Hannon, *Nuclear Instruments and Methods in Physics Research Section A: Accelerators, Spectrometers, Detectors and Associated Equipment*, 2005, **551**, 88–107.
- 18 A. K. Soper, *GudrunN and GudrunX : programs for correcting raw neutron and X-ray diffraction data to differential scattering cross section*, Rutherford Appleton Laboratory Technical Report RAL-TR-2011-013, 2011.
- 19 O. Arnold, J. C. Bilheux, J. M. Borreguero, A. Buts, S. I. Campbell, L. Chapon, M. Doucet, N. Draper, R. F. Leal, M. A. Gigg,

V. E. Lynch, A. Markvardsen, D. J. Mikkelsen, R. L. Mikkelsen, R. Miller, K. Palmen, P. Parker, G. Passos, T. G. Perring, P. F. Peterson, S. Ren, M. A. Reuter, A. T. Savici, J. W. Taylor, R. J. Taylor, R. Tolchenov, W. Zhou and J. Zikovsky, *Nuclear Inst. and Methods in Physics Research, A*, 2014, **764**, 156–166.

- 20 A. C. Larson and R. B. Von Dreele, *General Structure Analysis System (GSAS)*, Los Alamos National Laboratory Technical Report LAUR 86-748, 2004.
- 21 B. H. Toby, *Journal of Applied Crystallography*, 2001, **34**, 210–213.
- 22 M. Basham, J. Filik, M. T. Wharmby, Chang, P.C.Y., B. El Kassaby, M. Gerring, J. Aishima, K. Levik, B. C. A. Pulford, I. Sikharulidze, D. Sneddon, M. Webber, S. S. Dhesi, F. Maccherozzi, O. Svensson, S. Brockhauser, G. Naray and A. W. Ashton, *J. Synchrotron Rad* (2015). **22**, 853–858 [doi:10.1107/S1600577515002283], 2015, 1–6.
- 23 A. K. Soper and E. R. Barney, *J. Appl. Cryst* (2011). **44** [doi:10.1107/S0021889811021455], 2011, 1–13.
- 24 D. A. Keen, *Journal of Applied Crystallography*, 2001, **34**, 172–177.
- 25 M. T. Dove, M. G. Tucker and D. A. Keen, *European Journal of Mineralogy*, 2002, **14**, 331–348.
- 26 E. Lorch, *Journal of Physics C: Solid State Physics*, 1969, **2**, 229–237.
- 27 A. K. Soper and E. R. Barney, *Journal of Applied Crystallography*, 2012, **45**, 1314–1317.
- 28 R. L. McGreevy and L. Pusztai, *Molecular Simulation*, 1988, **1**, 359–367.
- 29 D. A. Keen, M. G. Tucker and M. T. Dove, *Journal of Physics: Condensed Matter*, 2005, **17**, S15–S22.



- 30 S. Adams and J. Swenson, *Physical Review Letters*, 2000, **84**, 4144–4147.
- 31 J. Swenson and S. Adams, *Physical Review B*, 2001, **64**, 281–10.
- 32 S. Adams, *Solid State Ionics*, 2002, **154-155**, 151–159.
- 33 S. Adams and J. Swenson, *Journal of Physics: Condensed Matter*, 2005, **17**, S87–S101.
- 34 M. G. Tucker, D. A. Keen, M. T. Dove, A. L. Goodwin and Q. Hui, *Journal of Physics: Condensed Matter*, 2007, **19**, 335218–16.
- 35 M. T. Dove and G. Rigg, *Journal of Physics: Condensed Matter*, 2013, **25**, 454222–9.
- 36 I. T. Todorov, W. Smith, K. Trachenko and M. T. Dove, *Journal of Materials Chemistry*, 2006, **16**, 1911–8.
- 37 M. Parrinello and A. Rahman, *Physical Review Letters*, 1980, **45**, 1196–1199.
- 38 S. Melchionna, G. Ciccotti and B. Lee Holian, *Molecular Physics*, 2006, **78**, 533–544.
- 39 S. Nosé, *The Journal of Chemical Physics*, 1984, **81**, 511–10.
- 40 W. G. Hoover, *Physical Review A*, 1985, **31**, 1695–1697.